

1 Identification of hidden population structure in
2 time-scaled phylogenies

3 Erik M. Volz^{1,*}, Carsten Wiuf², Yonatan H. Grad³, Simon D.W.
4 Frost^{4,5}, Ann M. Dennis⁶, and Xavier Didelot⁷

5 ¹*Department of Infectious Disease Epidemiology and MRC Centre for Global
6 Infectious Disease Analysis, Imperial College London*

7 ²*Department of Mathematical Sciences, University of Copenhagen*

8 ³*Department of Immunology and Infectious Diseases, TH Chan School of Public
9 Health, Harvard University*

10 ⁴*Department of Veterinary Medicine, University of Cambridge*

11 ⁵*The Alan Turing Institute*

12 ⁶*School of Medicine, University of North Carolina Chapel Hill*

13 ⁷*School of Life Sciences and Department of Statistics, University of Warwick*

14 * *Corresponding author: Norfolk Place, W2 1PG, United Kingdom; E-mail:
15 e.volz@imperial.ac.uk*

16

Abstract

Population structure influences genealogical patterns, however data pertaining to how populations are structured are often unavailable or not directly observable. Inference of population structure is highly important in molecular epidemiology where pathogen phylogenetics is increasingly used to infer transmission patterns and detect outbreaks. Discrepancies between observed and idealised genealogies, such as those generated by the coalescent process, can be quantified, and where significant differences occur, may reveal the action of natural selection, host population structure, or other demographic and epidemiological heterogeneities. We have developed a fast non-parametric statistical test for detection of cryptic population structure in time-scaled phylogenetic trees. The test is based on contrasting estimated phylogenies with the theoretically expected phylodynamic ordering of common ancestors in two clades within a coalescent framework. These statistical tests have also motivated the development of algorithms which can be used to quickly screen a phylogenetic tree for clades which are likely to share a distinct demographic or epidemiological history. Epidemiological applications include identification of outbreaks in vulnerable host populations or rapid expansion of genotypes with a fitness advantage. To demonstrate the utility of these methods for outbreak detection, we applied the new methods to large phylogenies reconstructed from thousands of HIV-1 partial *pol* sequences. This revealed the presence of clades which had grown rapidly in the recent past, and was significantly concentrated in young men, suggesting recent and rapid transmission in that group. Furthermore, to demonstrate the utility of these methods for the study of antimicrobial resistance, we applied the new methods to a large phylogeny reconstructed from whole genome *Neisseria gonorrhoeae* sequences. We find that population structure detected using these methods closely overlaps with the appearance and expansion of mutations conferring antimicrobial resistance.

48 Quantifying the role of population structure in shaping genetic
49 diversity is a longstanding problem in population genetics. When information
50 about how lineages are sampled is available, primarily geographic location, a
51 variety of statistics are available for describing the magnitude and role of
52 population structure (Hartl et al. 1997). In pathogen phylogenetics, such
53 geographic ‘meta-data’ has been instrumental in enabling the inference of
54 transmission rates over space (Dudas et al. 2017), host species (Lam et al.
55 2015), and even individual hosts (De Maio et al. 2018). Population structure
56 shapes genetic diversity, but can the existence of structure be inferred directly
57 from genetic data in the absence of structural covariates associated with each
58 lineage, such as if the geographic location or host species of a lineage is
59 unknown?

60 The problem of detecting and quantifying such ‘cryptic’ population
61 structure has become a pressing issue in several areas of microbial
62 phylogenetics. For example, in bacterial population genomics studies, a wide
63 diversity of methods have been recently developed to classify taxonomic units
64 based on distributions of genetic relatedness (Mostowy et al. 2017; Tonkin-Hill
65 et al. 2019, 2018; Beugin et al. 2018). In a different domain, pathogen
66 sequence data have been used for epidemiological surveillance, and ‘clustering’
67 patterns of closely related sequences have been used to aid outbreak
68 investigations and prioritise public health interventions (Eyre et al. 2012;
69 Dennis et al. 2014; Miller et al. 2014; Ledda et al. 2017). In both population
70 genomics studies and outbreak investigations, a common thread is the absence
71 of variables about sampled lineages that can be correlated with phylogenetic
72 patterns. For example, in outbreak investigations, host risk behaviour and
73 transmission patterns are not usually observed and must be inferred. It is not
74 known a priori which clades are more or less likely to expand in the future,

75 although there is active research addressing this problem, such as to predict
76 the emergence of strains of influenza A virus (Klingen et al. 2018) or the
77 forecast the effect of antibiotic usage policies on the prevalence of resistant
78 variants (Whittles et al. 2017).

79 In time-scaled phylogenies, the effects of population structure often
80 appear as a difference in the distribution of branch lengths in clades circulating
81 in different populations (Dearlove and Frost 2015). Figure 1 shows a simulated
82 genealogy from a structured coalescent process (Notohara 1990). In two clades,
83 the effective population size grows exponentially, and in the remaining clade,
84 the effective size remains constant. Consequently, the lineages through time
85 show noticeably different patterns of relatedness. For the clades with growing
86 size, most coalescent events occur in the distant past when the size was small.

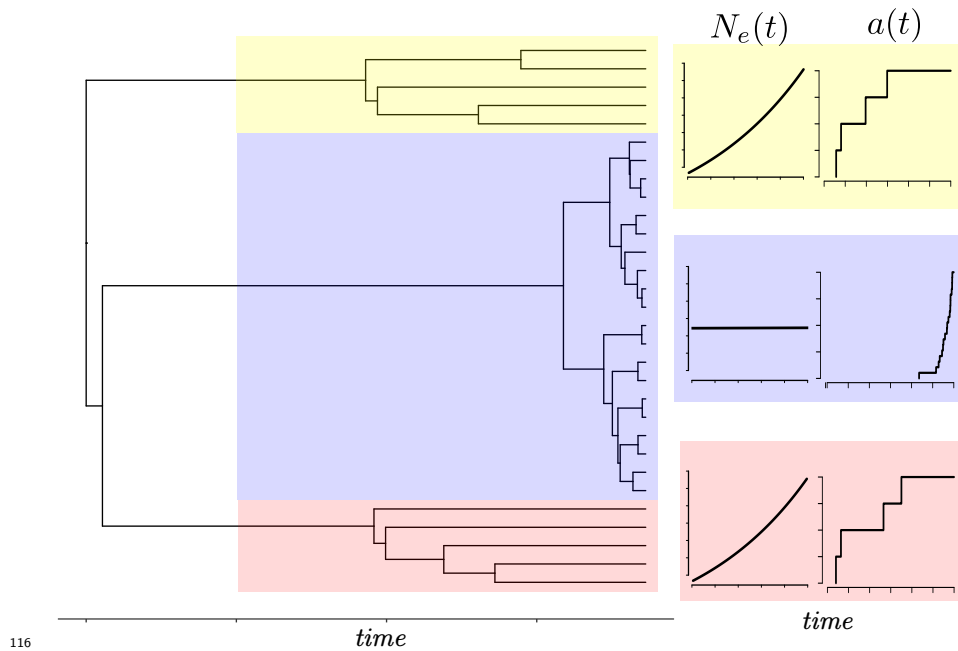
87 Supposing that the deme from which lineages were sampled was not
88 observed, it is clear from visual inspection of Figure 1 which lineages were
89 sampled from a growing population. Nevertheless, there is a paucity of
90 objective methods readily available to automate the process of identifying
91 temporally distinct clades. This process cannot be done manually when the
92 differences in distributions are less obvious, and needs to be based on a
93 theoretically grounded statistical test. Furthermore, in Figure 1, the red and
94 yellow clades are distantly related. Their most recent common ancestor
95 (MRCA) is at the root of the tree, but they have a very similar distribution of
96 coalescent times suggesting that they were generated by similar demographic
97 or epidemiological processes. For example, this can happen in infectious
98 disease epidemics, when lineages independently colonise the same host
99 population with greater susceptibility or higher risk behaviour (Dearlove et al.
100 2017). It is therefore also desirable to have an automated method for
101 identifying polyphyletic taxonomic groups defined by shared inferred

102 population histories as opposed to genetic or phenotypic traits.

103 Here we develop a statistical test for detecting if clades within a
104 time-scaled genealogy have evidence for unobserved population structure. Our
105 approach is to develop a statistic based on an unstructured coalescent process.
106 This allows us to test a null hypothesis that two clades are both generated by
107 the same coalescent process. In this case, the coalescent model provides a
108 theoretical prediction of the order of the coalescent times between the two
109 clades in the absence of population structure. On the basis of this statistical
110 test, we also develop algorithms for systematically exploring possible partitions
111 of a genealogy into distinct sets representing evolution within latent
112 populations with different demographic or epidemic histories. Notably, these
113 algorithms not only allow us to detect outlying clades with very different
114 genealogical patterns, but also to find and classify distantly related clades
115 which likely have similar demographic or epidemic histories.

124 **Materials and Methods**

125 As a starting point for our methodology, we assume a time-scaled phylogeny
126 has been estimated from genetic data, for example using one of the recently
127 developed fast methods (To et al. 2016; Volz and Frost 2017; Didelot et al.
128 2018; Sagulenko et al. 2018; Tamura et al. 2018; Miura et al. 2019).
129 Alternatively, summary trees obtained from full Bayesian approaches as
130 implemented in BEAST (Suchard et al. 2018; Bouckaert et al. 2014) or
131 RevBayes (Höhna et al. 2016) can be used, although these typically
132 incorporate population genetic models which presume a particular form of
133 population structure or a lack of population structure. Some precise
134 terminology and notation is required related to the structure of these
135 time-scaled trees since the basis of our approach concerns comparisons



117 Figure 1: A genealogy simulated from a structured coalescent process with two
118 demes, one of which has constant effective population size (clade highlighted
119 in blue), and the other having effective population size growing exponentially
120 (clades highlighted in red and yellow). Migration of lineages occurs at a small
121 constant rate in one direction from the constant size deme to the growing deme.
122 The corresponding plots at the right show a caricature of the effective population
123 size and lineages through time in each clade.

136 between different subsets of the tree.

137 Notation

138 The tree has n terminal nodes (nodes with no descendants), is rooted, and is
139 bifurcating (there are $n - 1$ internal nodes each with exactly two descendants).

140 Being rooted implies there is one node with no ancestor. Mathematically we
141 describe this tree as a node-labelled directed acyclic graph:

$$\mathcal{G} = (\mathcal{N}, \mathcal{E}, \tau)$$

142 where \mathcal{N} is a set of $2n - 1$ nodes, $\mathcal{E} \subseteq \{(u, v) | u, v \in \mathcal{N}^2\}$ is the set of $2n - 2$
143 edges or ‘lineages’, and $\tau: \mathcal{N} \rightarrow \mathbb{R}_{\geq 0}$ defines the time of each node. With
144 reference to an edge $(u, v) \in \mathcal{E}$ we say that u is the ‘direct ancestor’ and v is
145 the ‘direct descendant’ and we require $\tau(u) < \tau(v)$. Nodes are further
146 classified into two sets: ‘tips’ (terminal nodes) denoted \mathcal{T} with no descendants
147 and internal nodes denoted \mathcal{I} with exactly two direct descendants. The trees
148 may be heterochronous, meaning that tips of the tree can represent samples
149 taken at different time points.

150 For a node $u \in \mathcal{N}$ we define the clade C_u to be the set of nodes
151 descending from u , that is, the node u and all $v \in \mathcal{N}$ such that there is a
152 directed path of edges from u to v . We say that nodes v in C_u are ‘descended
153 from’ u . We will also have occasion to define clades ‘top down’ in terms of a
154 subset of tips in the tree. For this, we define the most recent common ancestor
155 $\text{MRCA}(X)$ of a set $X \subseteq \mathcal{T}$ to be the most recent node u such that $X \subseteq C_u$,
156 that is, all other nodes v with $X \subseteq C_v$ have $\tau(v) < \tau(u)$. Then we let the
157 top-down clade B_X be defined as

$$B_X = \{u \in \mathcal{N} \mid C_u \cap X \neq \emptyset\}.$$

158 Note that B_X includes the tips X as well as some nodes ancestral to
159 $\text{MRCA}(X)$.

160 In general $B_X \neq C_{\text{MRCA}(X)}$ since X does not necessarily include all
161 tips descending from $\text{MRCA}(X)$. We will also need to refer to the nodes
162 corresponding to coalescent events among lineages of the set X only, excluding
163 those between lineages of X and lineages of the complement of X ,

$$D_X = X \cup \{u \in B_X \mid \exists(u, v), (u, w) \in \mathcal{E}, v \neq w, C_v \cap X \neq \emptyset, C_w \cap X \neq \emptyset\},$$

164 Figure 2A illustrates a tree and the sets B_X , D_X , and $C_{\text{MRCA}(X)}$.

165 Since each node has a time, we can define the set of ‘extant’ lineages
166 $\mathcal{A}(t)$ at a particular time t to be the set of nodes occurring after time t with a
167 direct ancestor before time t ,

$$\mathcal{A}(t) = \{v \in \mathcal{N} \mid \exists(u, v) \in \mathcal{E}, \tau(u) < t \leq \tau(v)\}.$$

168 We might also refer to the number of extant lineages at time t , $a(t) = |\mathcal{A}(t)|$,
169 and if considering the number of extant lineages within a particular clade
170 ancestral to (and including) X we write

$$a_X(t) = |\mathcal{A}(t) \cap B_X|.$$

171 Non-parametric test for a given pair of clades

172 With the above notation, the rank-sum statistic can now be defined which will
173 form the basis for subsequent statistical tests and can be used to compare any
174 pair of clades in the tree.

175 Let X and Y represent disjoint sets of tips as represented in Figure
176 2B-D. Having sorted the nodes according to time and assigned a corresponding
177 rank to each internal node, this statistic computes the sum of ranks in a given
178 clade in comparison to a different clade:

$$\rho(X|Y) = \sum_{i=1}^K i \mathbf{1}_{D_X \setminus D_Y}(w_i), \quad (1)$$

179 where $S_{X,Y} = (w_1, w_2, \dots, w_K)$ is the sequence of internal nodes in $D_X \cup D_Y$
180 sorted by time (present to past), and $\mathbf{1}_A(u)$ is an indicator that takes the
181 value 1 if $u \in A$ and is zero otherwise. Note that $\rho(X|Y)$ is asymmetric in X
182 and Y . Also note that $\rho(X|Y)$ makes use of D_X, D_Y and not B_X, B_Y because
183 we are interested in the relative ordering of coalescent events among lineages
184 of X and Y . Only the ordering of the events matter, the absolute times are
185 immaterial to the test.

186 Under a neutral coalescent process, the distribution of coalescent
187 times in two clades ancestral to X and Y will depend on the number of extant
188 lineages through time in both clades and on the effective population size $N_e(t)$
189 (Wakeley 2009). However, the distribution of the relative ordering of
190 coalescent times only depends on the sizes of the clades. This distribution can
191 be computed rapidly by Monte-Carlo simulation as shown below, provided
192 that we know the probability that the next coalescent will be in X or Y as a
193 function of the number of lineages ancestral to X and Y , given by $a_X(t)$ and

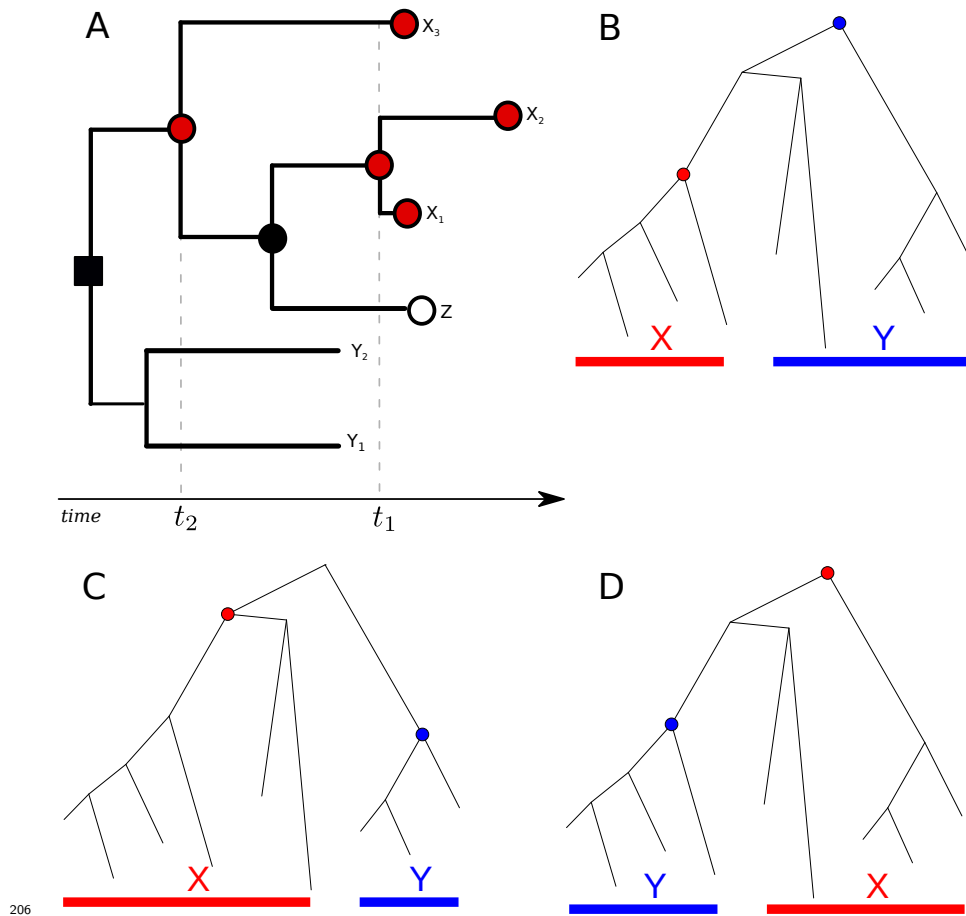
194 $a_Y(t)$. We here provide new theoretical results on the distribution of the
195 relative ordering of coalescence times under the null hypothesis that both B_X
196 and B_Y are clades within a single tree generated by a neutral unstructured
197 coalescent process. In the following we consider three different scenarios.

198 **Event E_1 .** Suppose that a clade B_X has a MRCA before any tip of X shares
199 a common ancestor with the clade of another set of tips Y , disjoint to X .
200 After lineages in X have found a common ancestor, the MRCA of X may or
201 may not coalesce with lineages in B_Y before Y has found a common ancestor.
202 Figures 2B-C illustrates trees that satisfies this condition. Note that in Figure
203 2B, a lineage in Y coalesces with the MRCA of X before lineages in Y find a
204 MRCA and in Figure B, both X and Y have a common ancestor before they
205 find a common ancestor with one another.

217 Observing a taxonomic pattern such as shown in Figures 2B-C is a
218 random event in a stochastic unstructured coalescent process, and we denote
219 this event by E_1 (suppressing X and Y for convenience). Wiuf and Donnelly
220 (Wiuf and Donnelly 1999) showed that the probability of observing E_1 , given
221 the state of the tree at a particular time t , only depends on the number of
222 lineages $z = a_X(t)$ and $w = a_Y(t)$,

$$Q_1(z, w) = \frac{2(z-1)!w!}{(z+w-1)!(z+1)}, \quad z, w \geq 1. \quad (2)$$

223 The numbers of extant lineages in B_X (or its complement) following
224 each coalescent event conditional on E_1 is a Markov chain. The transition
225 probabilities of this chain are exactly those needed to simulate the null
226 distribution of the test statistic $\rho(X|Y)$. The probability that the next
227 coalescent event is among lineages in the clade B_X given E_1 (starting at a
228 particular time t) and the current ancestral number of lineages of X , say z ,



206
 207 Figure 2: Coalescent trees for illustrating taxonomic relationships and notation
 208 used throughout the text. In panel A, the shape and colour of nodes correspond
 209 to variables B_X , D_X , and $C_{\text{MRCA}(X)}$ in relation to the set of tips $X =$
 210 $\{x_1, x_2, x_3\}$. All circles regardless of colour correspond to $C_{\text{MRCA}(X)}$. All filled
 211 shapes (red or black, square or circle) correspond to B_X . Note that this includes
 212 nodes ancestral to the MRCA of X . All red filled circles correspond to D_X . Two
 213 coalescent events occur among nodes in D_X at times t_1 and t_2 . Panels B-D show
 214 a coalescent tree and examples of potential taxonomic relationships between two
 215 clades. Prior knowledge of taxonomic relationships between X and Y influences
 216 the probability that the next coalescent event will be observed in clade X .

229 and Y , say w , was found by Wiuf and Donnelly (Wiuf and Donnelly 1999):

$$(z, w) \mapsto (z - 1, w) \quad \text{with probability} \quad \frac{z + 1}{z + w}. \quad (3)$$

230 **Event E_2 .** We further derive analogous probabilities under slightly different
231 conditions. Suppose we have disjoint sets of tips, X and Y . Let all lineages in
232 X share a common ancestor before any share a common ancestor with Y and
233 vice versa, all lineages in Y share a common ancestor before any share a
234 common ancestor with tips in X . Figure 2C illustrates a tree and two clades
235 that satisfy this condition, which we denote by E_2 . As before, the number of
236 ancestors in B_X and B_Y will form a Markov chain, conditional on E_2 .

237 The probability that the next coalescent event is among lineages in
238 the clade B_X given E_2 at a particular time t and the current ancestral number
239 of lineages of X , $z = a_X(t)$, and Y , $w = a_Y(t)$, can be given as:

$$(z, w) \mapsto (z - 1, w) \quad \text{with probability} \quad \frac{z - 1}{z + w - 2}, \quad z, w \geq 1. \quad (4)$$

240 To see this, note that without conditioning on E_2 , the probability that
241 the next coalescent is among ancestral nodes in B_X is

$$\frac{z(z - 1)}{(z + w)(z + w - 1)}.$$

242 This is simply the ratio of the coalescent rates in B_X , which is $\binom{z}{2}/N_e(t)$, to
243 the rate in $B_X \cup B_Y$, which is $\binom{z+w}{2}/N_e(t)$. The effective population size is
244 homogenous through the tree by hypothesis of the statistical test, and it
245 cancels out in this ratio. The probability that the coalescent event would be

246 between the clades ancestral to X and Y would be

$$\frac{2zw}{(z+w)(z+w-1)}.$$

247 The probability $Q_2(z, w)$ of the event E_2 must fulfil the recursion,

$$\begin{aligned} (z+w)(z+w-1)Q_2(z, w) \\ = z(z-1)Q_2(z-1, w) + w(w-1)Q_2(z, w-1), \end{aligned} \quad (5)$$

248 where $z, w \geq 1$. If there is exactly one lineage in both B_X and B_Y , then

249 $Q_2(1, 1) = 1$. If there is one lineage remaining in B_X and $w > 1$ in V_Y , then

250 $Q_2(1, w)$ is the probability that the next $w - 1$ coalescent events only occur

251 between lineages in B_Y and do not include the single lineage ancestral to X .

252 The probability of the next coalescent event being in B_Y is the probability of

253 not selecting the B_X lineage when sampling two extant lineages without

254 replacement:

$$\begin{aligned} Q_2(1, w) &= \prod_{j=2}^w \left(\frac{j}{j+1} \right) \left(\frac{j-1}{j} \right) \\ &= \frac{2}{w(w+1)}, \quad w \geq 1. \end{aligned} \quad (6)$$

255 Similarly, $Q_2(z, 1) = \frac{2}{z(z+1)}$, $z \geq 1$. This recursion can be solved explicitly to

256 give

$$Q_2(z, w) = \frac{2z!w!}{(z+w)!(z+w-1)}, \quad z, w \geq 1. \quad (7)$$

257 Now the transition probability (Equation 4) can be defined in terms of the

258 rate of coalescence in B_X and B_Y and the probability of E_2 being satisfied

259 following the coalescent event:

$$(z, w) \mapsto (z - 1, w) \quad \text{with probability} \\ \frac{z(z - 1)Q_2(z - 1, w)}{z(z - 1)Q_2(z - 1, w) + w(w - 1)Q_2(z, w - 1)} = \frac{z - 1}{z + w - 2}. \quad (8)$$

260 **Event E_3 .** Finally, we consider an event that is a combination of the scenarios
 261 described by events E_1 and E_2 . We denote E_3 to be the event that all X have
 262 a MRCA before sharing a common ancestor with lineages of Y and/or *vice*
 263 *versa*, all lineages in Y have a MRCA before sharing an ancestor with lineages
 264 of X . The trees in Figures 2B-D satisfy this condition.

265 The probability of the event E_3 might be defined in terms of Q_1 and
 266 Q_2 given previously:

$$Q_3(z, w) = Q_1(z, w) + Q_1(w, z) - Q_2(z, w) \\ = \frac{2z!w!}{(z + w - 1)!} \left(\frac{1}{z(z + 1)} + \frac{1}{w(w + 1)} - \frac{1}{(z + w)(z + w - 1)} \right), \quad (9)$$

267 with $z = a_X(t)$ and $w = a_Y(t)$ being sample sizes at a particular time t , as

268 before. Note that Q_2 is subtracted once in this equation because the

269 taxonomic relationship described by E_2 is already included in E_1 . The

270 function Q_3 satisfies the same recursion as above (Equation 5) with slightly

271 different boundary conditions:

$$Q_3(1, w) = Q_3(z, 1) = 1, \quad z, w \geq 1.$$

272 Transition probabilities can be derived as above by substituting Q_3 for Q_2 in

273 Equation 8. The probability that the next coalescent event is among lineages

274 in D_X conditional on E_3 is

$$(z, w) \mapsto (z - 1, w) \quad \text{with probability} \quad \frac{(z - 1)R_{z-1,w}}{(z - 1)R_{z-1,w} + (w - 1)R_{w,z-1}}, \quad (10)$$

where

$$R_{z,w} = \frac{1}{z(z+1)} + \frac{1}{w(w+1)} - \frac{1}{(z+w)(z+w-1)}, \quad z, w \geq 1. \quad (11)$$

275 **Algorithms for detecting population structure**

276 The null distribution of the test statistic $\rho(X, Y)$ can be computed by
277 Monte-Carlo simulation using Equations 3, 4 or 10 depending on the
278 taxonomic constraints to be conditioned on. This can be computed given any
279 pair of disjoint clades X and Y . Algorithm 1 in the Supporting Information
280 provides the simulation procedure for computing the two-sided p-values of an
281 empirical measurement $\hat{R} = \rho(X, Y)$, and we denote these p-values $\xi(X, Y, R)$.
282 The algorithm works by simulating many replicates of the rank-sum statistic
283 conditional on the sets X, Y , and the taxonomic relationship between these
284 clades. Furthermore, the order of sampling events and coalescent events is part
285 of the data within a time-scaled phylogeny. Thus the simulation procedure
286 does not simulate coalescent trees per se, but rather the number of lineages
287 through time $a_X(t)$ and $a_Y(t)$ by proceeding from the most recent sample back
288 to the MRCA of clades X and Y . Upon visiting a node in the ordered
289 sequence of coalescent events, the algorithm selects at random a clade D_X or
290 D_Y for this event using the transition probabilities from Equations 3, 4 or 10.
291 Upon visiting a coalescent event, $a_X(t)$ or $a_Y(t)$ is incremented using the
292 observed clade membership of the sample at that time. The end result of of
293 this simulation procedure is a large set of replicate rank-sum statistics which
294 serves as a null distribution for comparison with the value computed from the

295 time-scaled phylogeny.

296 While in principle this test allows comparison of any pair of disjoint
297 clades, the number of possible comparisons is vast, and deriving a useful
298 summary of taxonomic structure requires additional heuristic algorithms.
299 These algorithms are designed to stratify clades into self-similar sets and to do
300 so in a computationally efficient manner. Algorithm 2 in the Supporting
301 Information identifies ‘cladistic outliers’, which are clades that have a
302 coalescent pattern that is different from the remainder of the tree. It performs
303 a single pre-order traversal of the tree and greedily adds clades to the partition
304 with the most outlying values of the test statistic. At each node u visited in
305 pre-order traversal, Algorithm 2 examines all descendants v in C_u and
306 compares C_v with to $C_u \setminus C_v$. If no outliers are found, the algorithm will desist
307 from searching C_u and the set of tips $C_u \cap \mathcal{T}$ will be added to the partition. If
308 at least one outlier is found in C_u , a search will begin on the biggest outlier
309 (smallest p-value computed using Algorithm 1). The final result of this
310 algorithm is a partition of m non-overlapping clades $M = \{X_1, \dots, X_m\}$.

311 In practice, it is often desirable to not compare very small clades
312 against one another or much larger clades, so additional parameters are
313 available to desist the pre-order traversal upon reaching a clade with few
314 descendants. It is also often of practical interest to only compare clades that
315 overlap in time to a significant extent, so yet another parameter is available to
316 desist from comparing a pair of clades if few lineages in the pair ever coexist at
317 any time.

318 Additional algorithms are required to detect polyphyletic relationships
319 as depicted in Figure 1 which arise if, for example, distantly related lineages
320 colonise the same area and have similar population dynamics or if
321 near-identical fitness-enhancing mutations occur independently on different

322 lineages. Figure 1 depicts two distantly related clades (yellow and red) with
323 similar population dynamics, and it is desirable to classify these as a single
324 deme based on shared population dynamic history. Algorithm 2 will partition
325 tips of the tree into distinct clades with monophyletic or paraphyletic
326 relationships, however an approach based on pre-order traversal of the tree can
327 not on its own arrive at a polyphyletic partition of the tree. Therefore we can
328 implement a final hierarchical clustering step in order to group similar clades
329 as follows:

- 330 1. For each distinct pair of clades X and Y in partition M , compute
331 $q_{XY} = \xi(X, Y, \hat{R}_{XY})$.
- 332 2. Convert the p-value into a measure of distance between all clades:
333 $d_{XY} = |F^{-1}(q_{XY})|$, where F^{-1} is the inverse Gaussian cumulative
334 distribution function (quantile function). Set $d_{XX} = 0$ for all X .
- 335 3. Perform a conventional hierarchical clustering using a threshold distance
336 $F^{-1}(1 - \alpha/2)$ for confidence level α . Various clustering algorithms can
337 be used at this point, and our software has implemented the ‘complete
338 linkage’ algorithm (Everitt et al. 2001).

339 Algorithms 1 and 2 as well as the final hierarchical clustering step are
340 implemented as an open source R package called *treestructure* available at
341 <https://github.com/emvolz-phylogenetics/treestructure>. The R
342 package supports parallelisation and includes facilities for tree visualisation
343 using the *ggtree* package (Yu et al. 2017). The package provides convenience
344 functions to output cluster and partition assignment for downstream statistical
345 analysis in R.

346 **Simulation studies**

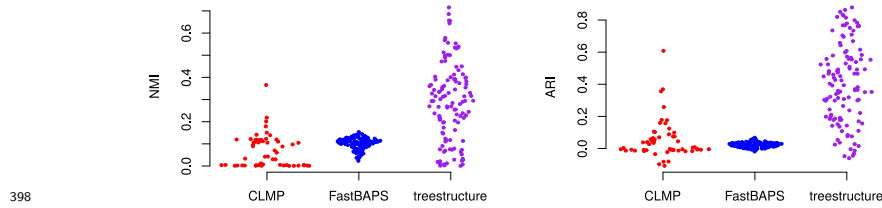
347 To evaluate the potential for *treestructure* to detect outbreaks we applied the
348 new method to phylogenies estimated from newly simulated data using a
349 structured coalescent model, as well as previously published simulation data
350 based on a discrete-event branching process (McCloskey and Poon 2017).

351 The structured coalescent simulation was based on a model with two
352 demes: a large deme with constant effective population size and a smaller
353 deme which grows exponentially up to the time of sampling. Migration occurs
354 at a constant rate in both directions between the growing and constant-size
355 demes, and equal proportions of these two demes are sampled. Coalescent
356 simulations were implemented using the *phydynR* package
357 <http://github.com/emvolz-phylogenomics/phydynR>. All genealogies
358 simulated from this model were comprised of 1000 tips with 200 of these
359 sampled from the growing deme. Each of 100 simulations were based on
360 different parameters such that there was a spectrum of difficulty identifying
361 population structure from the trees. The sample proportion was chosen
362 uniformly between 5% and 75% and, the growth rate in the growing deme was
363 chosen uniformly between 5% and 100% per year. Bidirectional migration
364 between demes was fixed at 5% per year. While most tips were sampled at a
365 single time point, 50 tips from the constant-size deme were distributed
366 uniformly through time in order to facilitate molecular clock dating. Multiple
367 sequence alignments were simulated based on trees using seq-gen (Rambaut
368 and Grass 1997). Each sequence comprised 1000 nucleotides from a HKY
369 model with a substitution rate of 10^{-3} per site per year. A neighbour joining
370 tree was estimated from each alignment and dated phylogenies estimated using
371 the *treedater* R package (Volz and Frost 2017) with a strict molecular clock.
372 The *treestructure* algorithm was applied to each phylogeny using the default

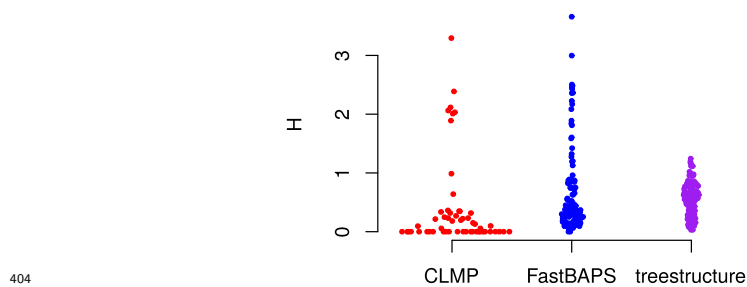
373 $\alpha = 1\%$ threshold.

374 Previously, McCloskey et al. simulated 100 genealogies from a
375 discrete-event birth-death process (McCloskey and Poon 2017; Vaughan and
376 Drummond 2013). These simulations were based on a process with
377 heterogeneous classes of individuals with different birth rates. With some
378 probability, lineages migrate to a class with higher birth rates. This could
379 represent a generic outbreak scenario such as a set of individuals with higher
380 risk behaviour or other exposures. In a separate set of simulations, the
381 outbreak population differs from the main population along multiple
382 dimensions: the birth rate and the sampling rate are both increased by a
383 common factor ($5\times$). 100 genealogies were simulated under both scenarios and
384 the *treestructure* algorithm was applied to each. To create more challenging
385 conditions for the method and to evaluate the sensitivity of the method to
386 sample coverage, we also applied the method to genealogies based on
387 subsampled lineages with a frequency of 25%. Complete descriptions of
388 parameters and simulation methods can be found in (McCloskey and Poon
389 2017).

390 The performance of *treestructure* was evaluated using the normalised
391 mutual information (NMI) statistic and adjusted Rand index (ARI) computed
392 using the *aricode* R package <https://github.com/jchiquet/aricode> (Vinh
393 et al. 2010). Both statistics quantify the strength of association between the
394 estimated and actual structure of the tree, with larger values corresponding to
395 higher quality reconstructions.



399 Figure 3: The normalised mutual information (NMI) and adjusted Rand index
400 (ARI) as a function of classifications from several tree-partitioning algorithms
401 and membership of lineages in outbreaks or a constant-size reservoir. Each point
402 corresponds to a structured coalescent simulation where 20% of tips are sampled
403 from an exponentially growing outbreak.



405 Figure 4: Entropy (H) of classification from several tree partitioning algorithms
406 applied to the structured coalescent simulations but only counting lineages
407 sampled from the exponentially growing outbreak.

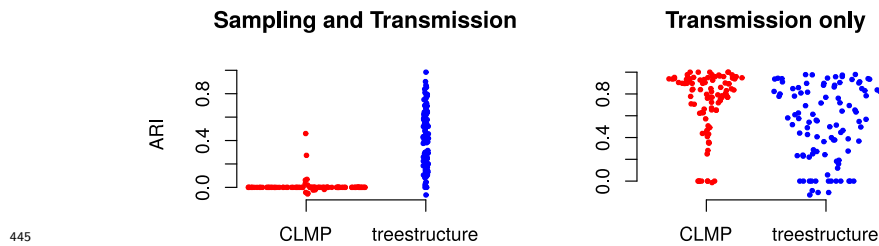
396 Results

397 Simulation studies

408 The *treestructure* algorithm achieves relatively high fidelity of classifications in
409 comparison to other methods in the structured coalescent simulations which
410 included 20% of samples from a rapidly growing outbreak. Figure 3 compares
411 three methods according to the NMI and ARI statistics. In these figures, the
412 partition of the tree computed by each method is compared to the true
413 membership of each sampled lineage in outbreak or in the constant-size
414 reservoir population. Across 100 simulations, *treestructure* has mean ARI of
415 41% (IQR: 20-57%). The FastBAPS method (Tonkin-Hill et al. 2019) has
416 mean ARI of 2.3% (IQR:1.2-3.3%) and the CLMP method (McCloskey and
417 Poon 2017) has mean ARI 5.2% (IQR:-1-7.5%).

418 The relatively lower performance of CLMP and FastBAPS in these
419 comparisons is largely a consequence of false-positive partitioning of samples
420 from the reservoir population, but CLMP and FastBAPS usually correctly
421 identify a clade that closely corresponds to the outbreak. In contrast, the
422 *treestructure* method seldom sub-divides clades from the reservoir. Figure 4
423 compares the entropy of partition assignments only within lineages sampled
424 from the outbreak. This shows that all methods are assigning outbreak
425 lineages to a small number of partitions and no method is clearly superior by
426 this metric. The CLMP method has the lowest entropy (mean 40%) but also
427 several large outliers. *treestructure* has higher entropy (mean 57%) but few
428 outliers, and FastBAPS is intermediate.

429 The performance of all methods depended on the sample density and
430 growth rate of the outbreak. Fast growing outbreaks are easier to detect by all
431 methods but the role of sample density is more ambiguous. The Pearson
432 correlation of ARI with growth rate is $\rho = 53\%$, 27% , 71% for *treestructure*,



446 Figure 5: The adjusted Rand index for 100 previously published simulations
447 (McCloskey and Poon 2017). This describes accuracy of classification of tips
448 into outbreaks using the *treestructure* method and CLMP. Results on left were
449 based on simulations where both transmission and sampling rates varied in the
450 outbreak cluster, whereas simulations on the right only allowed transmission
451 rates to vary.

433 CLMP and FastBAPS respectively. Not all methods are equally sensitive to
434 these parameters however and FastBAPS is especially sensitive to growth and
435 sample density. The growth rate and sample density collectively explain 41%,
436 28% and 60% of variance of ARI in *treestructure*, CLMP and FastBAPS
437 respectively.

438 We also performed analyses with Phydelity (Han et al. 2018) (results
439 not shown), a recently proposed method for transmission cluster identification.
440 This tended to generate a very large number of clusters, both within and
441 outside of the outbreak demes, reflecting a different emphasis of this method
442 on finding closely related clusters rather than addressing differences in
443 macro-level population structure. Thus, results with Phydelity and other
444 clustering methods were not easily comparable to *treestructure*.

452 Figure 5 shows performance of *treestructure* on previously published
453 tree simulations (McCloskey and Poon 2017). These simulations differ from
454 the structured coalescent simulations because both the reservoir and outbreak
455 demes are growing exponentially at different rates. The birth rate in the

456 outbreak deme is 5-fold the birth rate in the reservoir, but in one set of
457 simulations, both the birth rate and sampling rate in the outbreak was also
458 increased 5-fold. In these simulations, the performance of *treestructure*
459 (median ARI 56%) is slightly lower than the CLMP method (McCloskey and
460 Poon 2017) (median ARI 83%) when only the birth-rate differs in the
461 outbreak deme. However *treestructure* maintains good performance when
462 death and sampling rates also differ. In that case, *treestructure* has median
463 ARI 42% and CLMP has median ARI 0%. The difficulty of detecting
464 outbreaks with different sampling patterns was previously highlighted as a
465 challenge for CLMP (McCloskey and Poon 2017).

466 **Clonal expansion of drug-resistant *N. gonorrhoeae***

467 We examined the role of evolution of antimicrobial resistance in shaping the
468 phylogenetic structure of *N. gonorrhoeae* using 1102 previously described
469 whole genome sequences (Grad et al. 2016). These isolates were collected from
470 multiple sites in the United States between 2000 and 2013 and featured clonal
471 expansion of lineages with antibiotic resistance to different classes of
472 antibiotics. We estimated a maximum likelihood tree using *PhyML* (Guindon
473 et al. 2010) and corrected for the distorting effect of recombination using
474 *ClonalFrameML* (Didelot and Wilson 2015). We estimated a rooted
475 time-scaled phylogeny using *treedater* (Volz and Frost 2017). A relaxed clock
476 model was inferred, with a mean rate of 4.6×10^{-6} substitutions per site per
477 year. *BactDating* (Didelot et al. 2018) was also applied for the same purpose
478 and found to give very similar estimates for the clock rate and dating of clades.

479 We focus on the origin and expansion of two clades which
480 independently developed resistance to cefixime (CFX) by acquiring the mosaic
481 *penA* XXXIV allele (Grad et al. 2016). These clades are indicated in Figure 6.

482 Note, however, that the level of susceptibility to CFX varies, particularly in
483 the larger of these two clades. In one lineage within this clade, the mosaic
484 *penA* XXXIV allele was replaced by recombination with an allele associated
485 with susceptibility. Other isolates within this clade gained mutations that
486 further modified the extent of resistance. The larger of these two clades
487 emerged on a genomic background that is resistant to ciprofloxacin (CIP), so
488 that it has reduced susceptibility to both CIP and CFX. The smaller of the
489 two clades is resistant to CFX but not CIP. We therefore extracted a tree with
490 just 576 tips, representing the genomes from these two CFX-resistant clades as
491 well as genomes from the two clades that are most closely related to the two
492 CFX-resistant clades. The output of *treestructure* is shown in Figure 6, using
493 unique colours to highlight each of the 11 clusters that were identified with
494 $\alpha = 1\%$. The clusters reported by *treestructure* are highly correlated with
495 CFX resistance. Among all distinct pairs of sampled isolates, 84% share the
496 same resistance profile and cluster membership.

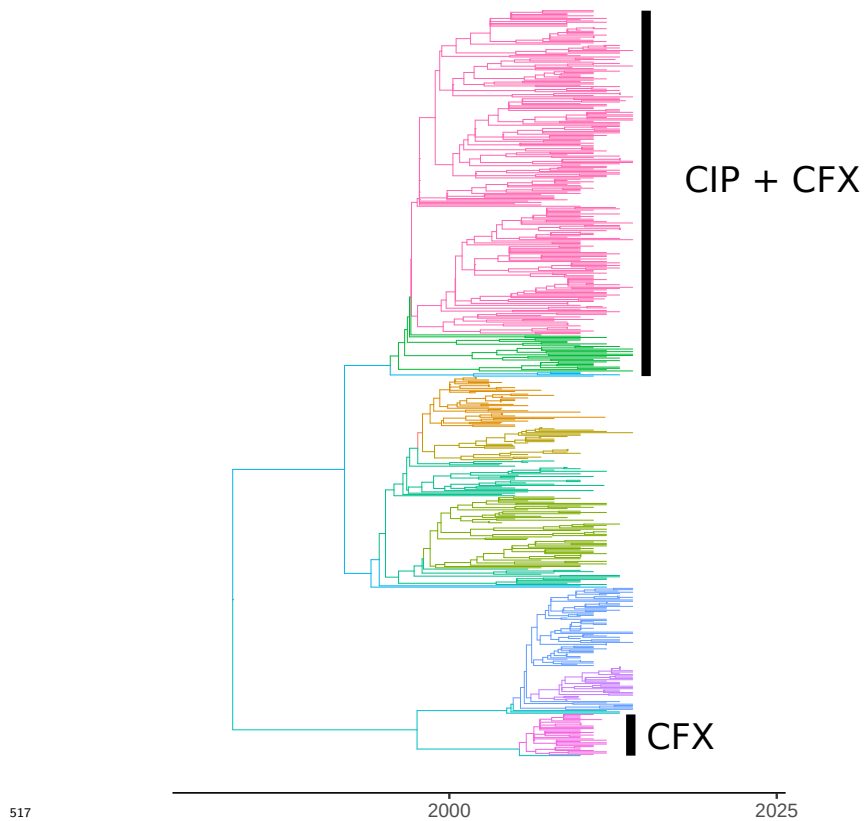
497 We compared *treestructure* with a different method for detecting
498 community structure, FastBAPS (Tonkin-Hill et al. 2019), since BAPS models
499 are often applied to bacterial pathogens. We applied FastBAPS using the
500 same time-scaled phylogeny described previously and using a trimmed
501 sequence alignment consisting of 38830 polymorphic sites and removing sites
502 with many gaps. This produced a similar partition of the tree (Figure S2)
503 with a few differences: FastBAPS clusters overlap exactly with the clade
504 featuring dual resistance (CIP and CFX), whereas *treestructure* classified a
505 small number of deep-splitting lineages into a different cluster. Note however
506 that this behaviour is not necessarily problematic, and may represent a
507 progressive increase in fitness following the acquisition of resistance through
508 the evolution of compensatory mutations (Didelot et al. 2016). On the other

509 hand, FastBAPS failed to identify the smaller clade with resistance to CFX
510 and not CIP and instead grouped that clade with its drug-sensitive sister
511 clade. In general, *treestructure* found many more clusters within the sister
512 clades and FastBAPS tended to group these together. We also applied the
513 much more computationally intensive RhierBAPS method (Tonkin-Hill et al.
514 2018), and obtained almost identical results to FastBAPS. Overall, BAPS
515 methods appear to give greater weight to long internal branches when
516 identifying clusters than *treestructure*.

523 **Epidemiological transmission patterns of HIV-1**

524 We reanalysed a time-scaled phylogeny reconstructed from 2068 partial *pol*
525 HIV-1 subtype B sequences collected from Tennessee between 2001 and 2015
526 (Dennis et al. 2018). Each lineage within this phylogeny corresponds to a
527 single HIV patient sampled at a single time point, and various clinical and
528 demographic covariate data concerning these patients can be associated with
529 each lineage. In the original study, these sequence data were used to show high
530 rates of transmission among young (age < 26.4) men who have sex with men
531 (MSM) (Dennis et al. 2018). Clustering by threshold genetic distance is often
532 used in HIV epidemiology (Dennis et al. 2014) and indicated that young white
533 MSM had the highest odds of clustering.

534 We applied the *treestructure* algorithm with default settings to the
535 time-scaled tree which yielded ten partitions with sizes ranging from 58 to 398.
536 The tree and partitions are shown in Figure 7 where partitions are labeled
537 according to the median year of birth among patients in each partition. Many
538 of these partitions were polyphyletic, suggesting possible multiple importations
539 of lineages to specific risk groups. We then compared the estimated partition
540 of the tree with patient covariates. A particular partition stands out along



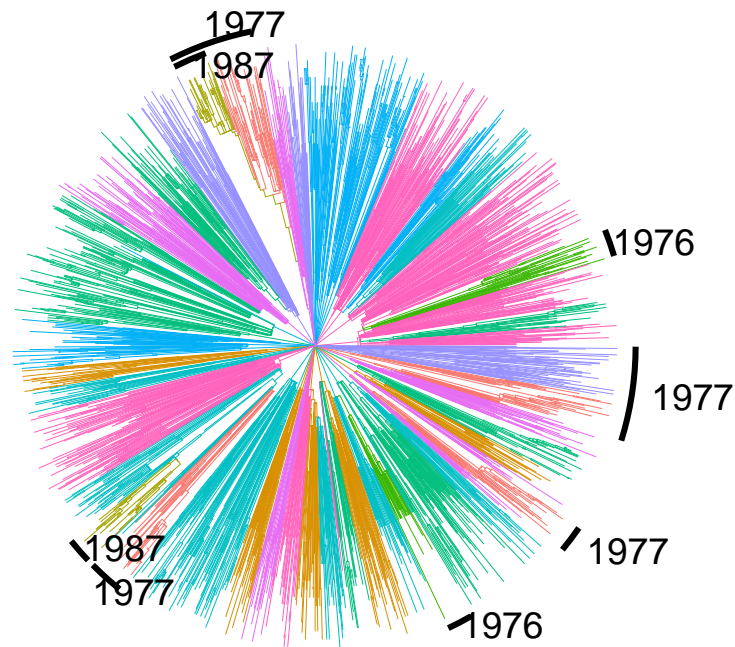
517

518 Figure 6: A time-scaled phylogeny based on 576 whole genomes of *N.*
519 *gonorrhoeae*, comprising two clades with reduced susceptibility to cefixime
520 (CFX) and their two sister clades. The top clade also has resistance to
521 ciprofloxacin (CIP). Different colours on the tree represent the partition detected
522 using the *treestructure* algorithm.

541 multiple dimensions: it is the smallest (size 58), polyphyletic, arose in the
542 recent past, and is characterised by very young MSM. The median year of
543 birth in this partition is 1987, in stark contrast to the rest of the sample with
544 year of birth in the 1970s. Clades within this young partition are also nested
545 paraphyletically under other relatively young partitions (cf. Figure 7).

546 We did not find a significant association between the tree partition
547 and residential postal codes (Tukey analysis of variance, $p = 0.097$). This is in
548 agreement with the original study which found minimal impact of geography
549 on genetic clustering in this sample, however this is largely a consequence of
550 the highly concentrated nature of the sample around Nashville. The ethnicity
551 of patients (black, white, and other) was strongly associated with the
552 estimated partition. Black MSM were strongly concentrated in the 1987
553 partition in particular (83% in contrast to 26-38% in all other partitions). The
554 odds ratio of black ethnicity given membership in the 1987 partition was 9.7
555 (95% CI:5.2-19.8).

562 Finally, we applied phylodynamic analysis methods to see if the
563 partition structure supported the previously published findings that young
564 MSM were transmitting at a higher rate (Dennis et al. 2018). To estimate N_e
565 through time, we used the nonparametric *skygrowth* R package (Volz and
566 Didelot 2018). We estimated $N_e(t)$ for each partition individually using a
567 range of precision parameters which control the smoothness (τ) of the
568 estimated trajectories since we lack a priori information about volatility of
569 these trajectories. Figure 8 shows $N_e(t)$ for each partition with $\tau = 10$ and
570 supporting Figures S3 and S4 show results using different values of τ . The
571 1987 partition again stands out as the only group which shows evidence of
572 recent and rapid population growth. Less dramatic recent periods of growth
573 are also noticeable for other partitions with young patients. The current



556

557 Figure 7: A time-scaled phylogeny estimated from HIV-1 *pol* sequences in
558 Tennessee (Dennis et al. 2018). The colours correspond to the ten partitions
559 identified using the *treestructure* algorithm. Several partitions are annotated
560 with the median year of birth of HIV patients from whom sequences were
561 sampled. Partitions lacking annotation had years of birth 1969-1972.

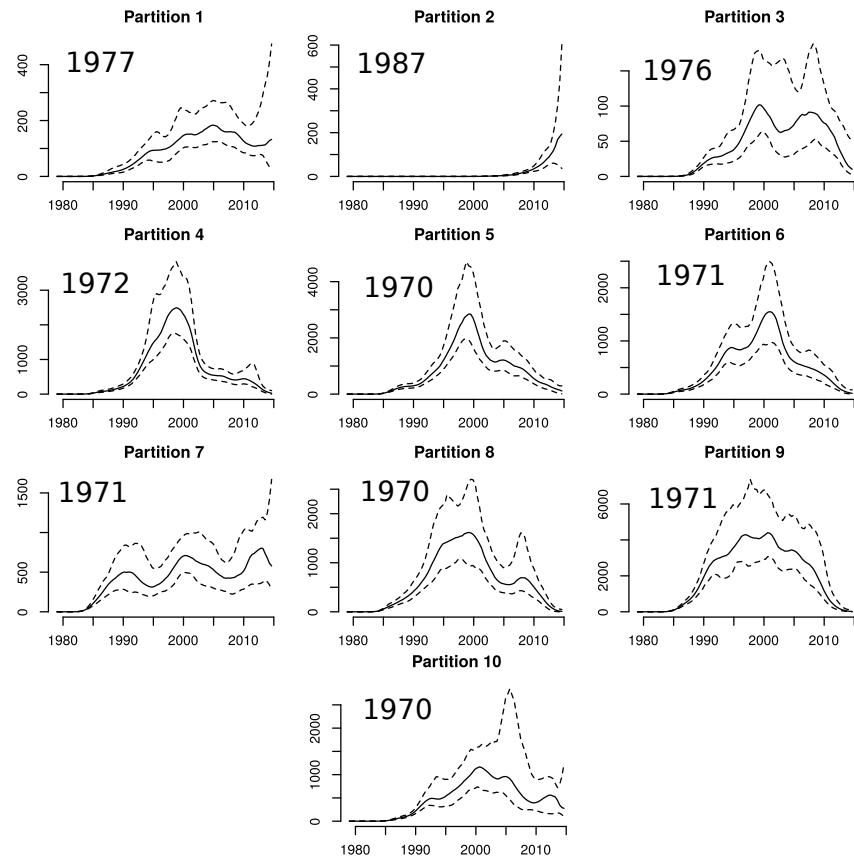
574 exponential growth in the 1987 partition is not consistent across all analyses,
575 but when $\tau < 10$ we find $N_e(t)$ drops precipitously in 2014-2015 (Figure S3).
576 However, this could also be an artefact of non-random sampling and inclusion
577 of transmission pairs within the sample.

583 This analysis supports the hypothesis that there has been a recent and
584 rapid rise of HIV transmissions among young MSM in Tennessee and in
585 particular among young black MSM. This interpretation is mostly in
586 agreement with the original study (Dennis et al. 2018), but we find that black
587 MSM are a group at greater risk than young white MSM.

588 Discussion

589 Contrasting the distribution of ordering of nodes provides a natural criterion
590 for distinguishing clades within a time-scaled phylogeny which are shaped by
591 different evolutionary or demographic processes. The non-parametric nature of
592 this classification method imposes minimal assumptions on the mechanisms
593 that generate phylogenetic patterns. Thus, we have found this method
594 maintains good performance over a diverse range of situations where
595 phylogenetic structure is produced, including differential transmission rates,
596 epidemiological outbreaks, evolution of beneficial mutations, and differential
597 sampling patterns. Our work is related to the research on species delimitation
598 methods (see for example (Zhang et al. 2013)) although targeted at
599 within-species variation, and is also related to recent work on methods for
600 detecting co-diversification of species(Oaks et al. 2019). This method appears
601 relatively robust compared to other methods against false-positive
602 identification of phylogenetic structure, but nevertheless has good sensitivity
603 for detecting structure in most situations.

604 There are many immediate applications of this method in the area of



578

579 Figure 8: Estimated effective population size through time for each partition in
580 the Tennessee HIV-1 phylogeny. Each panel is annotated with the median year
581 of birth among HIV patients in each partition. $N_e(t)$ was estimated using the
582 *skygrowth* method (Volz and Didelot 2018) with precision parameter $\tau = 10$.

605 pathogen evolution where time-scaled phylogenetics is increasingly used in
606 epidemiological investigations (Biek et al. 2015). We have demonstrated the
607 role of natural selection in shaping phylogenetic structure of *N. gonorrhoeae*,
608 and our method clearly identifies clades which expanded in the recent past due
609 to acquisition of antimicrobial resistance. We have demonstrated the role of
610 human demography and transmission patterns in shaping the evolution of
611 HIV-1, and our method has shown distinct outbreaks of HIV-1 in specific
612 groups defined by age, race, and behaviour. Furthermore, we have shown how
613 clades detected by this method can be analysed using phylodynamic methods
614 that can yield additional insights into recent outbreaks or the mechanisms
615 which generated phylogenetic structure. For example, we have applied
616 non-parametric methods to estimate the effective population size through time
617 in HIV outbreaks detected using *treestructure* which highlighted particular
618 groups that appear to be at higher risk of transmission. Such analyses would
619 be more problematic using other partitioning or clustering algorithms because
620 phylogenetic clusters can appear by chance in homogeneous populations of
621 neutrally evolving pathogens, and this can give the false appearance of recent
622 growth (Dearlove et al. 2017). This application of phylodynamics analysis
623 methods is possible because the statistical test used in *treestructure* provides
624 theoretical justification for treating each partition as a separate unstructured
625 population.

626 Applications of the *treestructure* algorithms are scalable to relatively
627 large phylogenies. The main algorithms require only a single pre-order
628 traversal of the tree and all of the computations presented here required less
629 than one minute to run. The method is based on a time-scaled phylogeny, and
630 the computational burden of this preliminary step is typically higher than that
631 of running *treestructure*, even though significant progress has been made

632 recently is this area (Volz and Frost 2017; Didelot et al. 2018; Sagulenko et al.
633 2018; Tamura et al. 2018; Miura et al. 2019). Future developments of
634 *treestructure* and other methods post-processing time-scaled phylogenies (Volz
635 and Didelot 2018; Didelot et al. 2017) should address the uncertainty in the
636 input phylogeny, for example by accounting for bootstrap or Bayesian support
637 values for phylogenetic splits, or by summarising results from multiple trees.

638 **Funding.** Research reported in this publication was supported by the
639 National Institute of Allergy and Infectious Diseases of the National Institutes
640 of Health under Award Number R01-AI135970 (EV, AD, SDWF). EV and XD
641 acknowledge funding from the UK Medical Research Council (MR/R015600/1)
642 and the National Institute for Health Research (NIHR) Health Protection
643 Research Unit in Modelling Methodology (HPRU-2012-10080). SDWF was
644 also supported in part by The Alan Turing Institute via an Engineering and
645 Physical Sciences Research Council Grant (EP/510129/1).

646 References

- 647 Beugin, M. P., T. Gayet, D. Pontier, S. Devillard, and T. Jombart. 2018. A
648 fast likelihood solution to the genetic clustering problem. *Methods Ecol.*
649 *Evol.* 9:1006–1016.
- 650 Biek, R., O. G. Pybus, J. O. Lloyd-Smith, and X. Didelot. 2015. Measurably
651 evolving pathogens in the genomic era. *Trends Ecol. Evol.* 30:306–313.
- 652 Bouckaert, R., J. Heled, D. Kühnert, T. Vaughan, C.-H. Wu, D. Xie, M. A.
653 Suchard, A. Rambaut, and A. J. Drummond. 2014. Beast 2: a software
654 platform for bayesian evolutionary analysis. *PLoS Comput. Biol.*
655 10:e1003537.
- 656 De Maio, N., C. J. Worby, D. J. Wilson, and N. Stoesser. 2018. Bayesian

- 657 reconstruction of transmission within outbreaks using genomic variants.
658 PLoS Comput. Biol. 14:e1006117.
- 659 Dearlove, B. L. and S. D. W. Frost. 2015. Measuring Asymmetry in
660 Time-Stamped Phylogenies. PLoS Comput. Biol. 11:e1004312.
- 661 Dearlove, B. L., F. Xiang, and S. D. Frost. 2017. Biased phylodynamic
662 inferences from analysing clusters of viral sequences. *Virus Evolution* 3.
- 663 Dennis, A. M., J. T. Herbeck, A. L. Brown, P. Kellam, T. de Oliveira,
664 D. Pillay, C. Fraser, and M. S. Cohen. 2014. Phylogenetic studies of
665 transmission dynamics in generalized HIV epidemics: an essential tool where
666 the burden is greatest? *J. Acquir. Immune Defic. Syndr.* 67:181–195.
- 667 Dennis, A. M., E. Volz, S. D. Frost, M. Hossain, A. F. Poon, P. F. Rebeiro,
668 S. H. Vermund, T. R. Sterling, and M. L. Kalish. 2018. Hiv-1 transmission
669 clustering and phylodynamics highlight the important role of young men
670 who have sex with men. *AIDS Research and Human Retroviruses*
671 34:879–888.
- 672 Didelot, X., N. J. Croucher, S. D. Bentley, S. R. Harris, and D. J. Wilson.
673 2018. Bayesian inference of ancestral dates on bacterial phylogenetic trees.
674 *Nucleic Acids Res.* 46:e134.
- 675 Didelot, X., C. Fraser, J. Gardy, and C. Colijn. 2017. Genomic infectious
676 disease epidemiology in partially sampled and ongoing outbreaks. *Mol. Biol.*
677 *Evol.* 34:997–1007.
- 678 Didelot, X., A. S. Walker, T. E. Peto, D. W. Crook, and D. J. Wilson. 2016.
679 Within-host evolution of bacterial pathogens. *Nat. Rev. Microbiol.*
680 14:150–162.

- 681 Didelot, X. and D. J. Wilson. 2015. ClonalFrameML: Efficient Inference of
682 Recombination in Whole Bacterial Genomes. *PLoS Comput. Biol.*
683 11:e1004041.
- 684 Dudas, G., L. M. Carvalho, T. Bedford, A. J. Tatem, G. Baele, N. R. Faria,
685 D. J. Park, J. T. Ladner, A. Arias, D. Asogun, F. Bielejec, S. L. Caddy,
686 M. Cotten, J. D'Ambrozio, S. Dellicour, A. Di Caro, J. W. Diclaro,
687 S. Duraffour, M. J. Elmore, L. S. Fakoli, O. Faye, M. L. Gilbert, S. M.
688 Gevao, S. Gire, A. Gladden-Young, A. Gnirke, A. Goba, D. S. Grant, B. L.
689 Haagmans, J. A. Hiscox, U. Jah, J. R. Kugelman, D. Liu, J. Lu, C. M.
690 Malboeuf, S. Mate, D. A. Matthews, C. B. Matranga, L. W. Meredith,
691 J. Qu, J. Quick, S. D. Pas, M. V. T. Phan, G. Pollakis, C. B. Reusken,
692 M. Sanchez-Lockhart, S. F. Schaffner, J. S. Schieffelin, R. S. Sealfon,
693 E. Simon-Loriere, S. L. Smits, K. Stoecker, L. Thorne, E. A. Tobin, M. A.
694 Vandi, S. J. Watson, K. West, S. Whitmer, M. R. Wiley, S. M. Winnicki,
695 S. Wohl, R. Wölfel, N. L. Yozwiak, K. G. Andersen, S. O. Blyden, F. Bolay,
696 M. W. Carroll, B. Dahn, B. Diallo, P. Formenty, C. Fraser, G. F. Gao, R. F.
697 Garry, I. Goodfellow, S. Günther, C. T. Happi, E. C. Holmes, B. Kargbo,
698 S. Keita, P. Kellam, M. P. G. Koopmans, J. H. Kuhn, N. J. Loman,
699 N. Magassouba, D. Naidoo, S. T. Nichol, T. Nyenswah, G. Palacios, O. G.
700 Pybus, P. C. Sabeti, A. Sall, U. Ströher, I. Wurie, M. A. Suchard, P. Lemey,
701 and A. Rambaut. 2017. Virus genomes reveal factors that spread and
702 sustained the ebola epidemic. *Nature* 544:309–315.
- 703 Everitt, B., S. Landau, and M. Leese. 2001. *Cluster Analysis*. Wiley New York.
- 704
- 705 Eyre, D. W., T. Golubchik, N. C. Gordon, R. Bowden, P. Piazza, E. M. Batty,
706 C. L. C. Ip, D. J. Wilson, X. Didelot, L. O'Connor, R. Lay, D. Buck, A. M.
707 Kearns, A. Shaw, J. Paul, M. H. Wilcox, P. J. Donnelly, T. E. A. Peto, A. S.

- 708 Walker, and D. W. Crook. 2012. A pilot study of rapid benchtop sequencing
709 of *Staphylococcus aureus* and *Clostridium difficile* for outbreak detection
710 and surveillance. *BMJ Open* 2:e001124.
- 711 Grad, Y. H., S. R. Harris, R. D. Kirkcaldy, A. G. Green, D. S. Marks, S. D.
712 Bentley, D. Trees, and M. Lipsitch. 2016. Genomic epidemiology of
713 gonococcal resistance to extended-spectrum cephalosporins, macrolides, and
714 fluoroquinolones in the united states, 2000–2013. *The Journal of Infectious*
715 *Diseases* 214:1579–1587.
- 716 Guindon, S., J.-F. Dufayard, V. Lefort, M. Anisimova, W. Hordijk, and
717 O. Gascuel. 2010. New algorithms and methods to estimate
718 maximum-likelihood phylogenies: assessing the performance of PhyML 3.0.
719 *Systematic Biology* 59:307–21.
- 720 Han, A., E. Parker, S. Maurer-Stroh, and C. Russell. 2018. Inferring putative
721 transmission clusters with phydelity. bioRxiv Page 477653.
- 722 Hartl, D. L., A. G. Clark, and A. G. Clark. 1997. Principles of population
723 genetics vol. 116. Sinauer associates Sunderland, MA.
- 724 Höhna, S., M. J. Landis, T. A. Heath, B. Boussau, N. Lartillot, B. R. Moore,
725 J. P. Huelsenbeck, and F. Ronquist. 2016. Revbayes: Bayesian phylogenetic
726 inference using graphical models and an interactive model-specification
727 language. *Systematic Biology* 65:726–736.
- 728 Klingen, T. R., S. Reimering, C. A. Guzmán, and A. C. McHardy. 2018. In
729 silico vaccine strain prediction for human influenza viruses. *Trends in*
730 *microbiology* 26:119–131.
- 731 Lam, T. T.-Y., B. Zhou, J. Wang, Y. Chai, Y. Shen, X. Chen, C. Ma,
732 W. Hong, Y. Chen, Y. Zhang, L. Duan, P. Chen, J. Jiang, Y. Zhang, L. Li,

- 733 L. L. M. Poon, R. J. Webby, D. K. Smith, G. M. Leung, J. S. M. Peiris,
734 E. C. Holmes, Y. Guan, and H. Zhu. 2015. Dissemination, divergence and
735 establishment of H7N9 influenza viruses in china. *Nature* 522:102–105.
- 736 Ledda, A., J. R. Price, K. Cole, M. J. Llewelyn, A. M. Kearns, D. W. Crook,
737 J. Paul, and X. Didelot. 2017. Re-emergence of methicillin susceptibility in a
738 resistant lineage of *Staphylococcus aureus*. *J. Antimicrob. Chemother.*
739 72:1285–1288.
- 740 McCloskey, R. M. and A. F. Poon. 2017. A model-based clustering method to
741 detect infectious disease transmission outbreaks from sequence variation.
742 *PLoS Comput. Biol.* 13:e1005868.
- 743 Miller, R., J. Price, E. Batty, X. Didelot, D. Wyllie, T. Golubchik, D. W.
744 Crook, J. Paul, T. E. A. Peto, D. J. Wilson, M. Cule, C. Ip, N. Day,
745 C. Moore, R. Bowden, and M. Llewelyn. 2014. Healthcare-associated
746 outbreak of methicillin-resistant *Staphylococcus aureus* bacteraemia: role of a
747 cryptic variant of an epidemic clone. *J. Hosp. Infect.* 86:83–89.
- 748 Miura, S., K. Tamura, S. L. K. Pond, L. A. Huuki, J. Priest, J. Deng, and
749 S. Kumar. 2019. A new method for inferring timetrees from temporally
750 sampled molecular sequences. *BioRxiv* Page 620187.
- 751 Mostowy, R., N. J. Croucher, C. P. Andam, J. Corander, W. P. Hanage, and
752 P. Marttinen. 2017. Efficient inference of recent and ancestral recombination
753 within bacterial populations. *Mol. Biol. Evol.* 34:1167–1182.
- 754 Notohara, M. 1990. The coalescent and the genealogical process in
755 geographically structured population. *J. Math. Biol.* 29:59–75.
- 756 Oaks, J. R., N. LBahy, and K. A. Cobb. 2019. Insights from a general,
757 full-likelihood bayesian approach to inferring shared evolutionary events

- 758 from genomic data: Inferring shared demographic events is challenging.
759 bioRxiv Page 679878.
- 760 Rambaut, A. and N. C. Grass. 1997. Seq-Gen: an application for the Monte
761 Carlo simulation of DNA sequence evolution along phylogenetic trees.
762 *Bioinformatics* 13:235–238.
- 763 Sagulenko, P., V. Puller, and R. A. Neher. 2018. Treetime:
764 Maximum-likelihood phylodynamic analysis. *Virus Evolution* 4:vex042.
- 765 Suchard, M. A., P. Lemey, G. Baele, D. L. Ayres, A. J. Drummond, and
766 A. Rambaut. 2018. Bayesian phylogenetic and phylodynamic data
767 integration using beast 1.10. *Virus Evolution* 4:vey016.
- 768 Tamura, K., Q. Tao, and S. Kumar. 2018. Theoretical foundation of the
769 RelTime method for estimating divergence times from variable evolutionary
770 rates. *Mol. Biol. Evol.* 35:1770–1782.
- 771 To, T.-H., M. Jung, S. Lycett, and O. Gascuel. 2016. Fast dating using
772 Least-Squares criteria and algorithms. *Systematic Biology* 65:82–97.
- 773 Tonkin-Hill, G., J. A. Lees, S. D. Bentley, S. D. W. Frost, and J. Corander.
774 2018. RhierBAPS: An R implementation of the population clustering
775 algorithm hierBAPS. *Wellcome Open Res* 3:93.
- 776 Tonkin-Hill, G., J. A. Lees, S. D. Bentley, S. D. W. Frost, and J. Corander.
777 2019. Fast hierarchical Bayesian analysis of population structure. *Nucleic
778 Acids Res.* Pages 1–11.
- 779 Vaughan, T. G. and A. J. Drummond. 2013. A stochastic simulator of
780 birth–death master equations with application to phylodynamics. *Molecular
781 biology and evolution* 30:1480–1493.

- 782 Vinh, N. X., J. Epps, and J. Bailey. 2010. Information theoretic measures for
783 clusterings comparison: Variants, properties, normalization and correction
784 for chance. *Journal of Machine Learning Research* 11:2837–2854.
- 785 Volz, E. M. and X. Didelot. 2018. Modeling the growth and decline of
786 pathogen effective population size provides insight into epidemic dynamics
787 and drivers of antimicrobial resistance. *Systematic Biology* 67:719–728.
- 788 Volz, E. M. and S. D. W. Frost. 2017. Scalable relaxed clock phylogenetic
789 dating. *Virus Evolution* 3.
- 790 Wakeley, J. 2009. *Coalescent theory: an introduction*. Greenwood Village:
791 Roberts & Company Publishers.
- 792 Whittles, L. K., P. J. White, and X. Didelot. 2017. Estimating the fitness
793 benefit and cost of cefixime resistance in *Neisseria gonorrhoeae* to inform
794 prescription policy: A modelling study. *PLoS Med.* 14:e1002416.
- 795 Wiuf, C. and P. Donnelly. 1999. Conditional genealogies and the age of a
796 neutral mutant. *Theor. Popul. Biol.* 56:183–201.
- 797 Yu, G., D. K. Smith, H. Zhu, Y. Guan, and T. T.-Y. Lam. 2017. ggtree: an r
798 package for visualization and annotation of phylogenetic trees with their
799 covariates and other associated data. *Methods in Ecology and Evolution*
800 8:28–36.
- 801 Zhang, J., P. Kapli, P. Pavlidis, and A. Stamatakis. 2013. A general species
802 delimitation method with applications to phylogenetic placements.
803 *Bioinformatics* 29:2869–2876.

Data: 1) Disjoint sets of tips X and Y
 2) Empirical value of test statistic \hat{R}
 3) Number of simulations n_{sim}
 4) Taxonomic condition E (see Equations 3, 4 or 10)
Result: Two-sided p-value denoted $q = \xi(X, Y, \hat{R})$.
 Initialisation;
 Form a time-ordered sequence of nodes

$$U = (u_1, \dots, u_{|D_X|+|D_Y|}) | u_i \in (D_X \cup D_Y), \tau(u_i) \geq \tau(u_{i+1})$$

Form a corresponding numeric sequence:

$\Upsilon = (v_1, \dots, v_{|D_X|+|D_Y|})$ where

$$v_i = \begin{cases} 1 & \text{if } u_i \in X \\ -1 & \text{if } u_i \in Y \\ 0 & \text{if } u_i \in (D_X \cup D_Y) \cap \mathcal{I} \end{cases}$$

for $k = 1$ to n_{sim} **do**
 $z \leftarrow 0$ (simulated lineages through time in clade X)
 $w \leftarrow 0$ (simulated lineages through time in clade Y)
 $r_{\text{sim}} \leftarrow 0$ (simulated rank-sum statistic)
 $c \leftarrow 0$ (number of coalescent events simulated)
 for $i = 1$ to $|D_X| + |D_Y|$ **do**
 if $v_i = 1$ **then**
 Account for sample in X : $z \leftarrow z + 1$;
 if $v_i = -1$ **then**
 Account for sample in Y : $w \leftarrow w + 1$;
 if $W_i = 0$ **then**
 Increment coalescent counter: $c \leftarrow c + 1$;
 Compute probability $\tilde{p} = \tilde{Q}_E(z, w)$ that next coalescent is in
 D_X or D_Y using Equation 3, 4 or 10;
 Draw a random uniform variable $\omega \leftarrow \text{Unif}(0, 1)$;
 if $\omega < \tilde{p}$ **then**
 $z \leftarrow z - 1$
 $r_{\text{sim}} \leftarrow r_{\text{sim}} + c$
 else
 $w \leftarrow w - 1$
 end
 Record simulated statistic:
 $R_k \leftarrow r_{\text{sim}}$
end

804

Compute number of simulations more and less than empirical value:

$$m_+ \leftarrow |\{r' \in R_k | r' > \hat{R}\}|$$

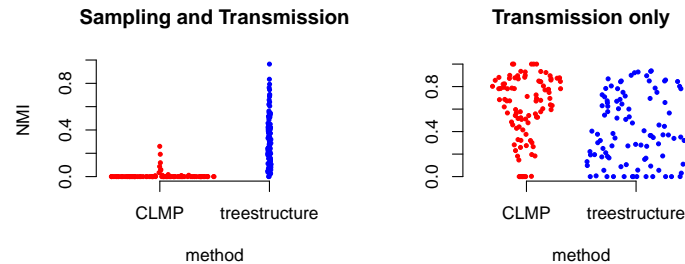
$$m_- \leftarrow |\{r' \in R_k | r' < \hat{R}\}|$$

Return $\min(\frac{m_+}{n_{\text{sim}}}, \frac{m_-}{n_{\text{sim}}})$.

Algorithm 1: Algorithm for computing the null distribution and associated p-value of the test-statistic for cladistic outliers.

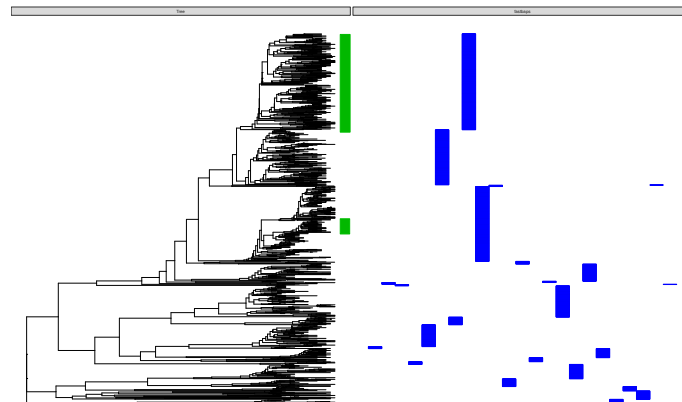
Data: Time-scale genealogy \mathcal{G}
Result: Partition of tips of tree, denoted M .
 Initialise ‘active set’ to consist of root node: $\Omega \leftarrow \{\text{root}\}$;
 Initialise partition: $M \leftarrow \emptyset$;
for $u \in \mathcal{I}$ (*internal nodes*) **do**
 | Initialise $\tilde{C}_u \leftarrow C_u$;
end
while $|\Omega| > 0$ **do**
 | Initialise $\Omega' \leftarrow \Omega$;
 | **for** $u \in \Omega$ **do**
 | | Find biggest outlier descended from u :
 | | $v^* \leftarrow \operatorname{argmax}_{v \in C_u} f(v) = \xi(\tilde{C}_u \setminus \tilde{C}_v, \tilde{C}_v)$ (Algorithm 1);
 | | $q \leftarrow \xi(\tilde{C}_u, \tilde{C}_{v^*})$;
 | | **if** $q < \alpha$ **then**
 | | | $\Omega' \leftarrow \Omega' \cup v^*$;
 | | | $\tilde{C}_u \leftarrow \tilde{C}_u \setminus C_{v^*}$;
 | | **else**
 | | | No significant outliers, so remove u from active sets:
 | | | $\Omega' \leftarrow \Omega' \setminus u$;
 | | | Add the clade descended from u to the partition:
 | | | $M \leftarrow M \cup \{\mathcal{T} \cap \tilde{C}_u\}$;
 | | **end**
 | **end**
 | $\Omega \leftarrow \Omega'$.
end
 Return M .
Algorithm 2: Algorithm for detecting cladistic outliers.

805



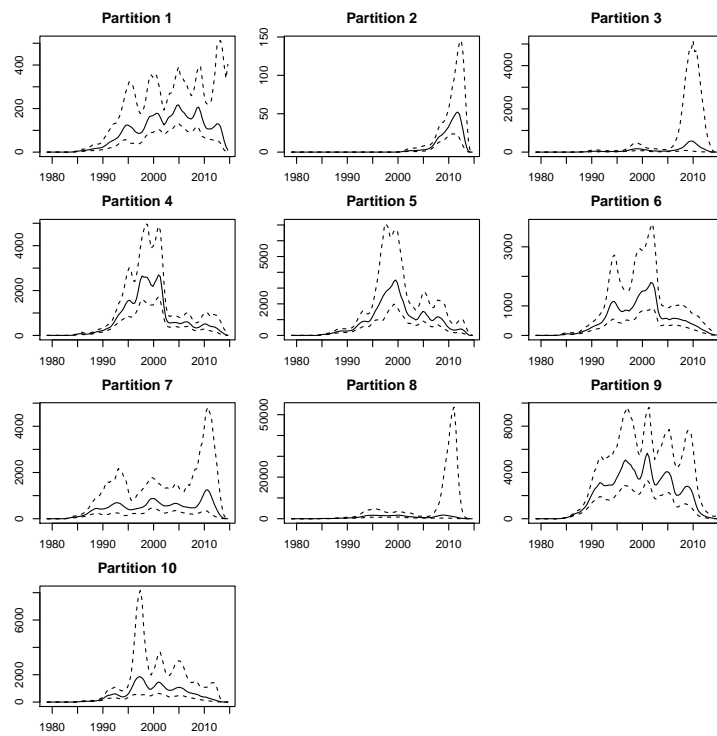
806

807 Figure S1: The normalised mutual information (NMI) for 100 previously
808 published simulations (McCloskey and Poon 2017). This describes accuracy of
809 classification of tips into outbreaks using the *treestructure* method and CLMP
810 (McCloskey and Poon 2017). Results on left were based on simulations where
811 both transmission and sampling rates varied in the outbreak cluster, whereas
812 simulations on the right only allowed transmission rates to vary.



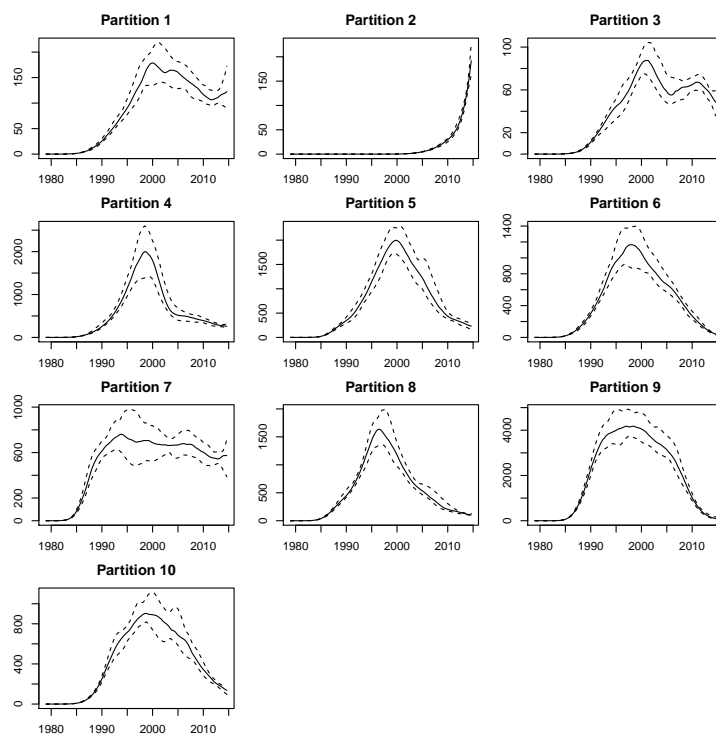
813

814 Figure S2: The output of FastBAPS classification applied to 1102 *N.*
815 *gonorrhoeae* isolates described in the main text. Clades indicated in green have
816 CFX resistance.



817

818 Figure S3: Estimated effective population size through time for each partition
819 in the Tennessee HIV-1 phylogeny. $N_e(t)$ was estimated using the *skygrowth*
820 method (Volz and Didelot 2018) with precision parameter $\tau = 1$.



821

822 Figure S4: Estimated effective population size through time for each partition
823 in the Tennessee HIV-1 phylogeny. $N_e(t)$ was estimated using the *skygrowth*
824 method (Volz and Didelot 2018) with precision parameter $\tau = 100$.